

Available online at [www.sciencedirect.com](http://www.sciencedirect.com)

**jmr&t**  
Journal of Materials Research and Technology  
[www.jmrt.com.br](http://www.jmrt.com.br)



## Original Article

# Computational and experimental investigation of refractory high entropy alloy $\text{Mo}_{15}\text{Nb}_{20}\text{Re}_{15}\text{Ta}_{30}\text{W}_{20}$

Uttam Bhandari<sup>a</sup>, Congyan Zhang<sup>a</sup>, Congyuan Zeng<sup>b</sup>, Shengmin Guo<sup>b</sup>,  
Shizhong Yang<sup>a,\*</sup>

<sup>a</sup> Department of Computer Science, Southern University and A&M College, Baton Rouge, LA, 70813, United States

<sup>b</sup> Department of Mechanical and Industrial Engineering, Louisiana State University, Baton Rouge, LA, 70803, United States



## ARTICLE INFO

## Article history:

Received 15 April 2020

Accepted 9 June 2020

## Keywords:

High entropy alloy

 $\text{Mo}_{15}\text{Nb}_{20}\text{Re}_{15}\text{Ta}_{30}\text{W}_{20}$ 

Mechanical property

Thermodynamic property

## ABSTRACT

In this study, refractory high entropy alloys (RHEAs)  $\text{Mo}_{20}\text{Nb}_{20}\text{Re}_{20}\text{Ta}_{20}\text{W}_{20}$ ,  $\text{Mo}_{15}\text{Nb}_{20}\text{Re}_{15}\text{Ta}_{30}\text{W}_{20}$ , and  $\text{Mo}_{15}\text{Nb}_{20}\text{Re}_{10}\text{Ta}_{35}\text{W}_{20}$  were studied by applying the first-principles density functional theory (DFT) method. The DFT calculation was based on a large unit cell model of 100-atom supercell, with randomly distributed five element atoms. The mechanical properties of all three RHEAs were calculated and compared. Comparing with the other two RHEAs,  $\text{Mo}_{15}\text{Nb}_{20}\text{Re}_{15}\text{Ta}_{30}\text{W}_{20}$  possesses balanced mechanical properties with an optimized concentration of expensive Re element. We combined the DFT calculations of a supercell with Debye–Grüneisen theory to investigate the thermal properties of the two RHEAs  $\text{Mo}_{20}\text{Nb}_{20}\text{Re}_{20}\text{Ta}_{20}\text{W}_{20}$  and  $\text{Mo}_{15}\text{Nb}_{20}\text{Re}_{15}\text{Ta}_{30}\text{W}_{20}$ .  $\text{Mo}_{15}\text{Nb}_{20}\text{Re}_{15}\text{Ta}_{30}\text{W}_{20}$  was selected for further experimental exploration and the computational results were compared. The experimental study shows the existence of a single BCC structure of  $\text{Mo}_{15}\text{Nb}_{20}\text{Re}_{15}\text{Ta}_{30}\text{W}_{20}$ . The crystal structure, density, lattice parameter, and hardness predicted computationally are consistent with the experiment data.

© 2020 The Author(s). Published by Elsevier B.V. This is an open access article under the CC BY license (<http://creativecommons.org/licenses/by/4.0/>).

## 1. Introduction

Metallic alloys other than traditional nickel-based superalloys with high hardness, high melting point, desirable ductility is often required by the aerospace industry and nuclear power reactor for high temperature applications. High entropy alloys (HEAs) have been proposed to meet the requirement of high temperature applications and extensively studied due to their single-phase microstructures and excellent mechanical properties. For example, many HEAs are hard [1], ductile [2], thermally resistant [3,4], fatigue resistant [5,6], and corrosion

resistant [7] in comparison with traditional alloys like Inconel 718 and Haynes 230. The extension of HEAs to refractory high entropy alloys (RHEAs) has been reported by Senkov et al. [3,8]. They found  $\text{MoNbTaW}$  and  $\text{MoNbTaVW}$  have higher melting points with good mechanical properties at high temperature compared to traditional alloys. Recently, other RHEAs such as  $\text{TaNbHfZrTi}$  [9],  $\text{TiZrNbTaMo}$  [10],  $\text{AlNbTiVZr}_x$  [11],  $\text{MoNbTaTiW}$  [12] have been extensively studied. These RHEAs possess a single body centered cubic (BCC) structure with magnificent mechanical properties than HEAs with face centered cubic (FCC) structure. However, some RHEAs like  $\text{NbCrMoTaTiZr}$  [13],  $\text{CrNbTiZr}$  [14] and  $\text{CrNbTiVZr}$  [15] shows the existence of Laves phase in BCC matrix because of small atomic size of Cr in those RHEAs. The precipitation of Laves phase affects the mechani-

\* Corresponding author.

E-mail: [shizhong.yang@subr.edu](mailto:shizhong.yang@subr.edu) (S. Yang).

<https://doi.org/10.1016/j.jmrt.2020.06.036>

2238-7854/© 2020 The Author(s). Published by Elsevier B.V. This is an open access article under the CC BY license (<http://creativecommons.org/licenses/by/4.0/>).

**Table 1 – Basic crystal structural properties of the RHEAs at RT.**

Alloys	$\Delta S_{mix}$ (J/K.mol)	$\Delta H_{mix}$ (kJ/mol)	$\delta$ (%)	$T_m$ (°C)	$\Omega$	VEC
Mo <sub>20</sub> Nb <sub>20</sub> Re <sub>20</sub> Ta <sub>20</sub> W <sub>20</sub>	13.38	–13.92	2.70	2945	2.83	5.8
Mo <sub>15</sub> Nb <sub>20</sub> Re <sub>15</sub> Ta <sub>30</sub> W <sub>20</sub>	13.08	–13.13	2.71	2956	2.94	5.65
Mo <sub>15</sub> Nb <sub>20</sub> Re <sub>15</sub> Ta <sub>35</sub> W <sub>20</sub>	12.68	–11.19	2.62	2947	3.33	5.55

cal properties of the RHEAs [16]. Thus, RHEAs with single BCC phase is essential for better mechanical properties.

The refractory high entropy alloy (RHEA) Mo<sub>20</sub>Nb<sub>20</sub>Re<sub>20</sub>Ta<sub>20</sub>W<sub>20</sub> was synthesized and evaluated by Bei in 2015 [17]. The existence of a BCC crystal structure was found in the experimental investigation. The reported modulus of Mo<sub>20</sub>Nb<sub>20</sub>Re<sub>20</sub>Ta<sub>20</sub>W<sub>20</sub> was 355 ± 15 GPa but the types of modulus was unknown. Other calculated phase diagram (CALPHAD) results [18,19] also showed the existence of a BCC phase in MoNbReTaW. To authors' knowledge, there were no any further theoretical or experimental study on mechanical and thermal properties of this alloy after discovery. For application purpose detailed study of structural, mechanical, and thermal properties is needed. Previous study shows that RHEAs whose composition are different from equimolar ratio have excellent mechanical properties [20–23].

In this study, equimolar concentration of RHEA MoNbReTaW were extended to non-equal molar RHEAs as Mo<sub>20</sub>Nb<sub>20</sub>Re<sub>20</sub>Ta<sub>20</sub>W<sub>20</sub>, Mo<sub>15</sub>Nb<sub>20</sub>Re<sub>15</sub>Ta<sub>30</sub>W<sub>20</sub>, and Mo<sub>15</sub>Nb<sub>20</sub>Re<sub>15</sub>Ta<sub>35</sub>W<sub>20</sub> to obtain high melting temperature, cost effective, balanced mechanical, and thermal properties. It is known that the melting point order of the five elements in this alloy system is W, Re, Ta, Mo, and Nb, in which Re is the most expensive element. Although W has the highest melting point, the concentration of W should be limited to 20% in the Ta contained alloys, according to the Smith group's report [24]. Therefore, the increase of the concentration of Ta is selected to achieve the alloy with a high melting point and Mo and Re was decreased to make the alloy highly solid by increasing the enthalpy and atomic radii. The empirical rule calculation predict that, all the three RHEAs will have single BCC solid solution as enthalpy of mixing [25]  $-15 \leq \Delta H_{mix} \leq 5$  kJ/mol, atomic size difference [26]  $\delta \leq 6.6\%$ , entropy of mixing [27]  $12 \leq \Delta S_{mix} \leq 17.5$  J/K•mol, and valence electron concentration VEC < 6.87 [28,29]. Calculated results are listed in Table 1.

We studied the mechanical properties of the RHEAs i.e. Mo<sub>20</sub>Nb<sub>20</sub>Re<sub>20</sub>Ta<sub>20</sub>W<sub>20</sub>, Mo<sub>15</sub>Nb<sub>20</sub>Re<sub>15</sub>Ta<sub>30</sub>W<sub>20</sub>, and Mo<sub>15</sub>Nb<sub>20</sub>Re<sub>15</sub>Ta<sub>35</sub>W<sub>20</sub> by first-principles density functional theory (DFT). The RHEA with least concentration of Re with balanced mechanical properties is selected for experimental verification.

## 2. Computational methods

The first-principles calculation was based on the DFT [30,31]. The Vienna ab-initio simulation package (VASP) [32] along with MedeA software [33] was used for the mechanical and thermal property calculations. The electron-ion interactions were described by the projector augmented wave (PAW) [34], while electron exchange-correlation interactions were described by the generalized gradient approximation

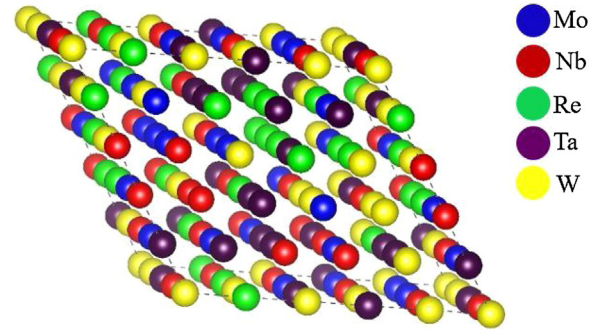


**Fig. 1 – The typical 100-atom random unit cell model of Mo<sub>20</sub>Nb<sub>20</sub>Re<sub>20</sub>Ta<sub>20</sub>W<sub>20</sub>.**

(GGA) [35] in the scheme of Perdew-Burke-Ernzerhof (PBE) [36]. The electronic iterations convergence was  $10^{-4}$  eV. Our model was spin unpolarized and a plane-wave cutoff energy of 500 eV was used. The requested k-spacing is 0.2 per Angstrom, which leads to a  $4 \times 3 \times 3$  mesh. This corresponds to actual k-spacings of  $0.172 \times 0.183 \times 0.183$  per Angstrom. We constructed the BCC structure of Mo<sub>15</sub>Nb<sub>20</sub>Re<sub>15</sub>Ta<sub>30</sub>W<sub>20</sub> that consisted of a 100-atom supercell model. The Knuth-Shuffle model [37] was utilized to distribute the five elements randomly using a Python code. Fig. 1 shows the supercells of Mo<sub>15</sub>Nb<sub>20</sub>Re<sub>15</sub>Ta<sub>30</sub>W<sub>20</sub>. More information about the 100-atom model can be found in the previous publication [38].

The elastic properties calculation was based on the stress-strain approach of Le Page and Saxe [39]. The current implementation in MedeA software is based on stress [40]. The relationship between applied elastic-strain ( $\epsilon_i$ )  $i=(1,6)$  and stress ( $c_{ij}$ ) is given below,

$$\sigma_i = \sum_{j=1}^6 C_{ij} \epsilon_j \quad (1)$$

where  $\epsilon_i$  is a tensor.

After finding the three independent elastic constants for a cubic crystal system i.e.,  $C_{11}$ ,  $C_{12}$ , and  $C_{44}$ , other elastic properties like bulk modulus  $B$ , shear modulus  $G$ , Young's modulus  $E$ , and Poisson's ratio  $\nu$  were calculated using Voigt-Reuss-Hill approximation [41] by the following equations:  $B = \frac{1}{3} (C_{11} + 2C_{12})$ ,  $G = \frac{1}{2} (G_{Voigt} + G_{Reuss})$ , where  $G_{Voigt} = \frac{1}{5} (C_{11} - C_{12} + 3C_{44})$  and  $G_{Reuss} = \frac{5}{4(S_{11} - S_{12}) + 3S_{44}}$ ,  $S$  is compliance matrix,

$$E = \frac{9BG}{3B+G} \text{ and } \nu = \frac{3B-2G}{2(3B+G)}. \quad (2)$$

The thermodynamic properties calculations are based on the Debye theory. The Grüneisen [42] constant  $\gamma_G$  was initially set to 2. After this,  $\gamma_G$  was derived from the pressure-volume

equation. A convenient approximation that was used to find out the  $\gamma_G$  parameter [43] is stated below,

$$E(v) = \frac{BV_0}{\frac{5}{6} - \gamma_G} \left( \frac{V}{V_0} \right)^{\frac{5}{6} - \gamma_G} \left( \ln \frac{V}{V_0} - \frac{1}{\frac{5}{6} - \gamma_G} \right) + E_\infty, \quad (3)$$

where  $V_0$  is equilibrium volume and  $B$  is bulk modulus.

The Debye temperature was obtained by using the formula of the mean sound velocity as follows:

$$\theta_D = \frac{\hbar}{K_B} \left( \frac{6\pi^2 q}{V_0} \right)^{\frac{1}{3}} V_m. \quad (4)$$

where  $q$  is the number of atoms in the unit cell,  $V_0$  its volume,  $\hbar$ , and  $K_B$  are Planks and Boltzmann constant respectively. The specific heat capacity,  $C_V$ , as a function of temperature,  $T$ , is estimated as,

$$C_{V(T)} = pq k_B \left( \frac{T}{\theta_D} \right)^3 \int_0^{\frac{x_D}{\theta_D}} \frac{x^4 \exp x}{(\exp x - 1)^2} dx. \quad (5)$$

The linear thermal expansion coefficient  $\alpha$  was calculated using the relation:

$$\alpha_L(T) = \frac{1}{3} \gamma_G \frac{C_V(T)}{BV_0}. \quad (6)$$

### 2.1. Experimental methods

The  $\text{Mo}_{15}\text{Nb}_{20}\text{Re}_{15}\text{Ta}_{30}\text{W}_{20}$  samples were synthesized using the arc melting method. To melt the samples, an arc melter (Edmund Bühler /MAM-1) was used under an argon atmosphere. As metal powders can easily be ejected from the arc region, Mo, Nb, Re, Ta, and W powders were first mixed and then pressed in an uniaxial stainless steel die to form disk shaped blocks. After loading the disk shaped samples into the arc-melter processing chamber, the arc-melter vacuum system would pull vacuum and then high purity argon gas would refill the chamber. Typically, the evacuation/refill process was repeated for at least three times to ensure a low residual oxygen level. With a proper chamber argon pressure ( $\sim 0.3$  bar), the arc was initiated to melt the sample. After melting completed, the arc was kept on for about 10 s. Then the melted sample solidifies to form a button shaped ingot. This ingot would be flipped over and the arc melting process was repeated for three more times. The repeated melting would ensure the chemical homogeneity within the ingots. The solid ingots were mounted into epoxy resin to make easy handling. The crystal structure of the sample was analyzed using a PANalytical Empyrean X-ray diffraction (XRD) system with 2 theta scan range from 20 to 120 degree. The X-ray used for the XRD test was generated from the anode material copper (Cu), and the used wavelength is K-Alpha 1 (1.54060 Å). The ingots were cut using a slow saw to show flat inner planes for microstructure and hardness examinations. Prior to the microstructure and hardness tests, the sample surfaces were mechanically ground using SiC papers with the grit size 320, 600, 800, 1000, and 1200 mesh sequentially, then polished with polycrystalline diamond suspension (6  $\mu\text{m}$ ,

3  $\mu\text{m}$ , and 1  $\mu\text{m}$  in sequence). The hardness characterization was performed with the SUN-TEC CM-802AT(V/K) hardness testing machine, 10 indents were conducted for each testing load to ensure the repeatability of the results. And the space between adjacent indents is over three times the indent diagonal length. To obtain the chemical composition, the samples were sectioned, polished, and cleaned first before loaded into a scanning electron microscope (SEM). Field emission scanning electron microscope equipped with second electron (SE) and energy dispersive spectroscopy (EDS) detector was used to examine the microstructure and the chemical compositions of the  $\text{Mo}_{15}\text{Nb}_{20}\text{Re}_{15}\text{Ta}_{30}\text{W}_{20}$  samples. We typically use area scan feature and multiple regions were measured to provide the averaged chemical compositions.

## 3. Results and discussions

### 3.1. Structural properties

The entropy ( $\Delta S_{\text{mix}}$ ), atomic size differences ( $\delta$ ), and enthalpy of mixing ( $\Delta H_{\text{mix}}$ ) were used to predict the solid-solution phase formation of RHEAs [44]. The calculated basic crystal structure properties of the RHEAs are shown in Table 1. A new parameter  $\Omega$  was coined by Zhang et al. [27], that uses  $\Delta S_{\text{mix}}$ ,  $\Delta H_{\text{mix}}$ , and melting temperature of mixing ( $T_m$ ) for predicting the solid solution phase formation in RHEAs. It is observed that  $\Omega > 1.10$  and  $\delta < 6.6\%$  are needed to form a solid solution [45]. According to the related VEC studies [29,30], the VEC of BCC phase RHEAs is less than 6.87. It can be seen from Table 1 that the VEC value of current RHEAs is less than 6.87, indicating that the RHEAs will have a BCC crystal phase. The calculated parameters from Table 1 suggest the existence of a stable solid BCC structure for all three RHEAs.

### 3.2. Mechanical properties

The calculated elastic constants and other mechanical properties of the current RHEAs are listed in Table 2. The DFT based calculation of elastic constants reveals that current RHEAs are elastically stable as ( $C_{44} > 0$ ,  $C_{11} > |C_{12}|$ , and  $C_{11} + 2C_{12} > 0$ ). The ductility and metallic characters of a material can be determined by the B/G ratio (Pugh's theory) [46] and the sign of the Cauchy pressure ( $C_{11} - C_{44}$ ) [47]. The conditions for ductility and metallic behavior of polycrystalline material are: (1) B/G ratio should be more than 1.75, and (2) a positive value of Cauchy pressure. Our calculation shows the B/G ratio is greater than 1.75 and Cauchy pressure is positive for all three RHEAs. It demonstrates the current RHEAs are ductile and possess metallic character. Moreover, Poisson's ratio of ductile material must be greater than 0.26 [48]. The value of  $\nu$  is greater than 0.26 for all three RHEAs which further confirms the ductile nature of them. We believe future ductility experiment will confirm our findings. The model proposed by Chen et al. [49] was implemented to find the Vickers hardness of the RHEAs. The Vickers hardness of  $\text{Mo}_{20}\text{Nb}_{20}\text{Re}_{20}\text{Ta}_{20}\text{W}_{20}$ ,  $\text{Mo}_{15}\text{Nb}_{20}\text{Re}_{15}\text{Ta}_{30}\text{W}_{20}$  and  $\text{Mo}_{15}\text{Nb}_{20}\text{Re}_{10}\text{Ta}_{35}\text{W}_{20}$  are estimated to be 8.88 GPa, 8.85 GPa, and 6.03 GPa, respectively. Our hardness calculation was based on Chen's model equation as  $H_v = 1.887 (K^2G)^{0.585}$ , where

**Table 2 – Calculated elastic constants (GPa);  $C_{11}$ ;  $C_{12}$ ;  $C_{44}$ , Cauchy pressure  $C_{11}-C_{44}$  (GPa), bulk modulus  $B$  (GPa), shear modulus  $G$  (GPa), Young's modulus  $E$  (GPa), Poisson's ratio ( $\nu$ ), Pugh's ratio ( $B/G$ ), lattice constant  $a$  (Å), density  $\rho$  (g/cm<sup>3</sup>) and hardness  $H_v$  (GPa). All calculations are in zero pressure and zero Kelvin temperature.**

Alloys	$C_{11}$	$C_{12}$	$C_{44}$	$C_{11}-C_{44}$	$B$	$G$	$E$	$\nu$	$B/G$	$\rho$	$a$	$H_v$
Mo <sub>20</sub> Nb <sub>20</sub> Re <sub>20</sub> Ta <sub>20</sub> W <sub>20</sub>	390	191	111	186	258	111	293	0.31	2.30	14.8	3.22	8.88
Mo <sub>15</sub> Nb <sub>20</sub> Re <sub>15</sub> Ta <sub>30</sub> W <sub>20</sub>	381	181	109	183	248	108	285	0.30	2.28	15.04	3.05	8.85
Mo <sub>15</sub> Nb <sub>20</sub> Re <sub>10</sub> Ta <sub>35</sub> W <sub>20</sub>	358	181	88	183	238	90	241	0.33	2.62	14.8	3.23	6.03

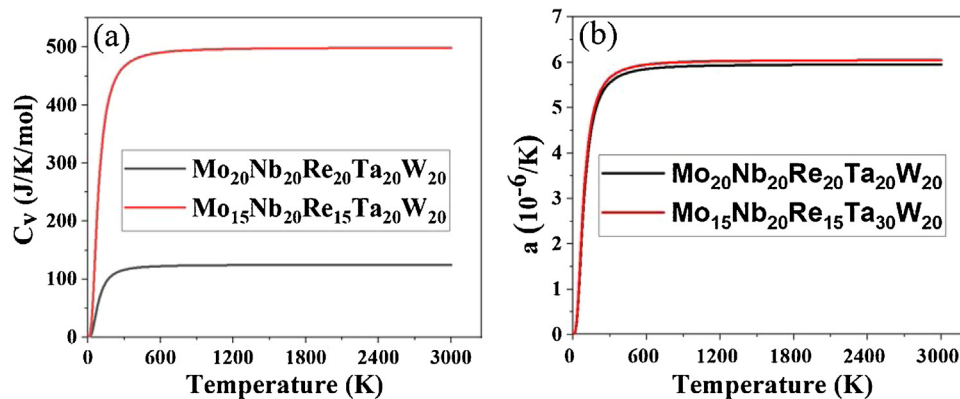


**Fig. 2 – (a) Variations of vibrational heat capacity ( $C_v$ ) with temperature (K) for Mo<sub>20</sub>Nb<sub>20</sub>Re<sub>20</sub>Ta<sub>20</sub>W<sub>20</sub> and Mo<sub>15</sub>Nb<sub>20</sub>Re<sub>15</sub>Ta<sub>30</sub>W<sub>20</sub>; (b) Variations of thermal coefficient of linear expansion ( $\alpha$ ) with temperature for Mo<sub>20</sub>Nb<sub>20</sub>Re<sub>20</sub>Ta<sub>20</sub>W<sub>20</sub> and Mo<sub>15</sub>Nb<sub>20</sub>Re<sub>15</sub>Ta<sub>30</sub>W<sub>20</sub>.**

$K=G/B$ . The addition of alloying element Ta along with the same amount reduction of Re element, expands the equilibrium volume of RHEAs: Mo<sub>15</sub>Nb<sub>20</sub>Re<sub>10</sub>Ta<sub>35</sub>W<sub>20</sub> (1693.29 Å<sup>3</sup>) > Mo<sub>15</sub>Nb<sub>20</sub>Re<sub>15</sub>Ta<sub>30</sub>W<sub>20</sub> (1676.88 Å<sup>3</sup>). This results in lowering of shear modulus of RHEAs: Mo<sub>15</sub>Nb<sub>20</sub>Re<sub>10</sub>Ta<sub>35</sub>W<sub>20</sub> < Mo<sub>15</sub>Nb<sub>20</sub>Re<sub>15</sub>Ta<sub>30</sub>W<sub>20</sub>. It is clear from Chen's model equation that the calculated hardness of alloy is directly proportional to the shear modulus. Therefore, Mo<sub>15</sub>Nb<sub>20</sub>Re<sub>10</sub>Ta<sub>35</sub>W<sub>20</sub> has the lowest shear modulus as compared with the other two RHEAs and has a low hardness. Since Re concentration is optimized with same Vickers hardness as of Mo<sub>20</sub>Nb<sub>20</sub>Re<sub>20</sub>Ta<sub>20</sub>W<sub>20</sub>, we select Mo<sub>15</sub>Nb<sub>20</sub>Re<sub>15</sub>Ta<sub>30</sub>W<sub>20</sub> for experimental studies.

### 3.3. Thermodynamics properties

The calculated mean sound velocity, Debye temperature, and Grüneisen parameter of Mo<sub>15</sub>Nb<sub>20</sub>Re<sub>15</sub>Ta<sub>30</sub>W<sub>20</sub> were 3010 m/s, 350.1 K, and 1.83 respectively. We did not study the thermal properties Mo<sub>15</sub>Nb<sub>20</sub>Re<sub>10</sub>Ta<sub>35</sub>W<sub>20</sub> as its predicted hardness is too low. Fig. 2(a) shows a plotted graph between temperature and the calculated vibrational heat capacity at constant volume ( $C_v$ ). The  $C_v$  value for both RHEAs rises exponentially at low temperatures (0–250) K and becomes linear at high temperature above 600 K. This linear increment of  $C_v$  is mostly caused by the lattice vibration and will reach the Dulong Petit limit at high temperatures. The  $C_v$  of Mo<sub>15</sub>Nb<sub>20</sub>Re<sub>15</sub>Ta<sub>30</sub>W<sub>20</sub> >  $C_v$  of Mo<sub>20</sub>Nb<sub>20</sub>Re<sub>20</sub>Ta<sub>20</sub>W<sub>20</sub>. This tendency implies that the addition of high melting point element Ta increases the  $C_v$  of Mo<sub>15</sub>Nb<sub>20</sub>Re<sub>15</sub>Ta<sub>30</sub>W<sub>20</sub>. It follows Mo<sub>15</sub>Nb<sub>20</sub>Re<sub>15</sub>Ta<sub>30</sub>W<sub>20</sub> can absorb more heat than Mo<sub>20</sub>Nb<sub>20</sub>Re<sub>20</sub>Ta<sub>20</sub>W<sub>20</sub> which may be effective in high temperature application. Fig. 2(b) shows the thermal coefficient of linear expansion ( $\alpha$ ) as

a function of temperature for Mo<sub>20</sub>Nb<sub>20</sub>Re<sub>20</sub>Ta<sub>20</sub>W<sub>20</sub> and Mo<sub>15</sub>Nb<sub>20</sub>Re<sub>15</sub>Ta<sub>30</sub>W<sub>20</sub>. For both cases of current RHEAs, the value of  $\alpha$  increases quickly at a temperature below 300 K after that  $\alpha$  increases slowly and becomes linear. Above 300 K, there is a slight increase in  $\alpha$  of Mo<sub>15</sub>Nb<sub>20</sub>Re<sub>15</sub>Ta<sub>30</sub>W<sub>20</sub> compared to the Mo<sub>20</sub>Nb<sub>20</sub>Re<sub>20</sub>Ta<sub>20</sub>W<sub>20</sub>. The addition of a high atomic radius element Ta with the reduction of low atomic radius elements Re and Mo in Mo<sub>15</sub>Nb<sub>20</sub>Re<sub>15</sub>Ta<sub>30</sub>W<sub>20</sub> may increase atomic strains in the RHEA, causing more lattice distortion, thus the slight increase of  $\alpha$  of Mo<sub>15</sub>Nb<sub>20</sub>Re<sub>15</sub>Ta<sub>30</sub>W<sub>20</sub>. The different values of  $\alpha$  and  $C_v$  for current RHEAs are listed in Table 3. To best of author's information, there is no any experimental and theoretical results on thermal properties of current RHEAs to make comparison. Therefore, the present findings can supply information for future studies.

### 3.4. Experimental results

XRD pattern of the studied Mo<sub>15</sub>Nb<sub>20</sub>Re<sub>15</sub>Ta<sub>30</sub>W<sub>20</sub> is shown in Fig. 3. It indicates the existence of single-phase BCC phase in Mo<sub>15</sub>Nb<sub>20</sub>Re<sub>15</sub>Ta<sub>30</sub>W<sub>20</sub>, which is consistent with our prediction from empirical parameter calculation. The wavelength of the X-ray is 1.5406 Å. With the diffraction pattern and Bragg's law [54], the lattice parameter was determined to be  $3.21 \pm 0.002$  Å. And this lattice parameter is very close to the predicted value of 3.224 Å.

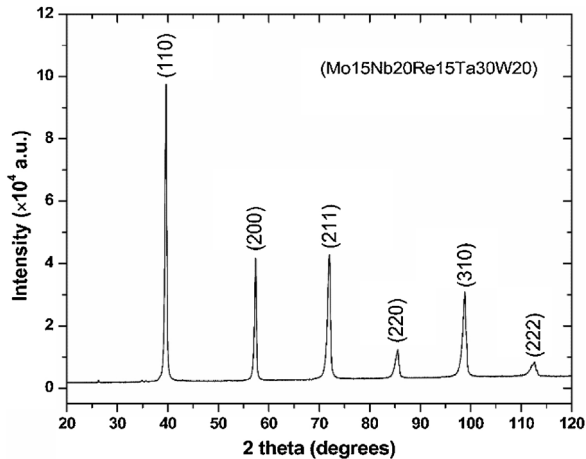
The measured density of Mo<sub>15</sub>Nb<sub>20</sub>Re<sub>15</sub>Ta<sub>30</sub>W<sub>20</sub> was 15.64 g/cm<sup>3</sup>. Using the mixture rule

$$\rho_{\text{mix}} = \sum C_i x_i \sqrt{\sum \frac{C_i x_i}{\rho_i}} \quad (7)$$



**Table 3 – Calculated vibrational heat capacity at constant volume  $C_V$  (J/K/mol) and thermal coefficient of linear expansion  $\alpha$  ( $10^{-5}/K$ ) for  $Mo_{20}Nb_{20}Re_{20}Ta_{20}W_{20}$  and  $Mo_{15}Nb_{20}Re_{15}Ta_{30}W_{20}$ .**

	Temperature (K)	$Mo_{20}Nb_{20}Re_{20}Ta_{20}W_{20}$	$Mo_{15}Nb_{20}Re_{15}Ta_{30}W_{20}$
$C_V$ (J/K/mol)	100	70.71	289.7
	300	116.27	466.62
	1500	124.39	497.66
	3000	124.66	498.68
$\alpha$ ( $10^{-6}/K$ )	100	3.37	3.51
	300	5.55	5.66
	1500	5.94	6.03
	3000	5.95	6.04

**Fig. 3 – X-ray diffraction patterns of as-cast  $Mo_{15}Nb_{20}Re_{15}Ta_{30}W_{20}$  alloy.****Table 4 – Experimental hardness test of  $Mo_{15}Nb_{20}Re_{15}Ta_{30}W_{20}$  RHEA.**

Load (gf)	Average hardness (GPa)	Standard Deviation (GPa)
2000	5.40	0.21
500	6.04	0.30
100	6.45	0.14

where  $C_i$  is the molar composition of an element,  $x_i$  is the atomic weight and  $\rho_i$  is the density of the pure element  $i$ , the estimated density is  $15.05 \text{ g/cm}^3$ . The measured density is slightly higher (0.06%) than the predicted one. This may be due to the possible minor evaporation of low melting point elements, like Mo and Nb. Vickers hardness was characterized with a digital micro hardness tester (Clark Instrument Model CM-802AT). Three testing loads were used, namely 2000, 500, and 100 gf, and the dwell time was 15 s. The Vickers microhardness ( $H_v$ ) of  $Mo_{15}Nb_{20}Re_{15}Ta_{30}W_{20}$  was tested at five different spots on the sample for each testing load and results are in Table 4.  $H_v$  is predicted from shear modulus and bulk modulus using the Chen et al. model [52]. This model does not consider any slip planes, plastic deformation, and lattice defects in the model system which results in an overestimation of the hardness than the corresponding experiment. Sarker et al. [50] also found a small disagreement of  $H_v$  between their prediction and experiment using Chen's Model in the RHEA  $HfNbTaTiVC_5$ . In addition, this value of hardness is greater than previously measured hardness

**Table 5 – EDS composition analysis results.**

Elements	Composition (at.%)	
	Average	Standard deviation
Mo	14.43	0.17
Nb	22.74	0.38
Re	15.29	0.009
Ta	26.66	0.19
W	20.90	0.19

of other HEAs such as,  $HfMoTaZr$  (5.31 GPa) [51],  $HfMoNbTaTiZr$  (4.95 HV) [52],  $AlCoCrFeNiVx$  (5.23 GPa) [52],  $NbMoTaW$  [3] (4.46 GPa), and  $MoNbTaTiW$  [8] (4.89 GPa).

The atomic percentages of the entire five scanned areas with point measurements and standard deviations are listed in Table 5. The average elemental ratio of the  $Mo_{15}Nb_{20}Re_{15}Ta_{30}W_{20}$  is determined by the EDS scan area. It shows the sample composition deviates slightly from the initial composition due to evaporation losses during the arc melting process. Fig. 4(a) shows the EDS chemical composition analysis areas of  $Mo_{15}Nb_{20}Re_{15}Ta_{30}W_{20}$  taken at 5 selected areas.

The elemental distribution in the sample is shown in the EDS mapping results, Fig. 5. Fig. 5(b–f) are the EDS mapping results of W, Re, Nb, Mo, and Ta over the area shown in Fig. 5(a). The dark regions shown in Fig. 5 are enriched with Nb, Mo, Ta, but are in deficiency of W and Re. It is noteworthy that, although two distinguishable parts with differing composition are observed on the sample surface (Figs. 4 and 5), according to the XRD patterns we got experimentally in Fig. 3, BCC is the only phase structure detected. Besides, at each diffraction angle, only single diffraction peak is observed, which indicates that despite the different composition, the lattice parameters of the matrix are quite close, and the variance is negligible.

The present findings of  $Mo_{15}Nb_{20}Re_{15}Ta_{30}W_{20}$  such as high hardness with stable single BCC structure and high melting point suggest that it could be a potential candidate for high-strength structure applications. Based on the first-principles calculation of the Poisson ratio, and the Pugh criterion, and the Cauchy pressure, we conclude that the  $Mo_{15}Nb_{20}Re_{15}Ta_{30}W_{20}$  is ductile. We hope the future experiment will confirm our ductility prediction and further emphasize the application of  $Mo_{15}Nb_{20}Re_{15}Ta_{30}W_{20}$ . The experimentally measured lattice parameter, density, and hardness of  $Mo_{15}Nb_{20}Re_{15}Ta_{30}W_{20}$  agree with computational prediction. This agreement also validates the reliability of our random 100-atom supercell. The computational model introduced in this study can be

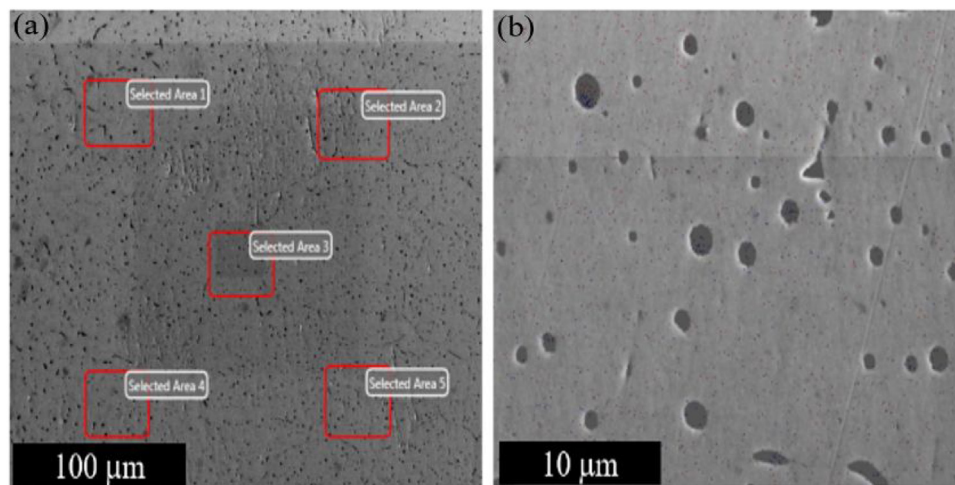


Fig. 4 – (a) EDS composition analysis areas of  $\text{Mo}_{15}\text{Nb}_{20}\text{Re}_{15}\text{Ta}_{30}\text{W}_{20}$ ; (b) SEM second electron region of  $\text{Mo}_{15}\text{Nb}_{20}\text{Re}_{15}\text{Ta}_{30}\text{W}_{20}$ .

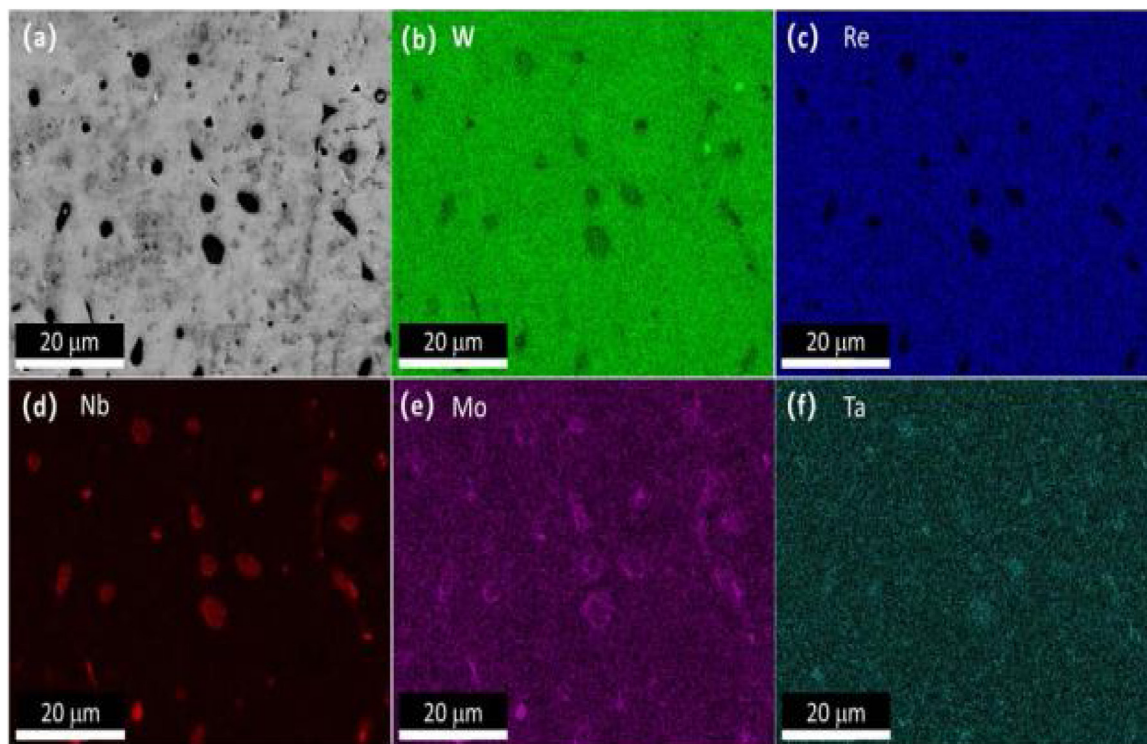


Fig. 5 – EDS mapping results of Nb, Mo, Ta, W, and Re of  $\text{Mo}_{15}\text{Nb}_{20}\text{Re}_{15}\text{Ta}_{30}\text{W}_{20}$ .

extended in predicting the mechanical properties of future RHEAs.

#### 4. Conclusions

In this computational and experimental study,  $\text{Mo}_{15}\text{Nb}_{20}\text{Re}_{15}\text{Ta}_{30}\text{W}_{20}$  was investigated. The experimental study showed the existence of a stable single-phase BCC crystal structure with a lattice constant of  $3.21 \pm 0.002 \text{ \AA}$ , a density of  $15.64 \text{ g/cm}^3$  and hardness ranging up to  $6.45 \text{ GPa}$  with a load of  $100 \text{ gf}$  for  $\text{Mo}_{15}\text{Nb}_{20}\text{Re}_{15}\text{Ta}_{30}\text{W}_{20}$ . These exper-

imentally found properties are in good agreement with the DFT prediction using 100 atoms supercell. The  $B/G$  ratio of  $\text{Mo}_{15}\text{Nb}_{20}\text{Re}_{15}\text{Ta}_{30}\text{W}_{20}$  was 2.28 which shows its ductile nature according to Pugh's theory. Based on the analysis of the graphs of thermal expansion coefficient and vibrational heat capacity,  $\text{Mo}_{15}\text{Nb}_{20}\text{Re}_{15}\text{Ta}_{30}\text{W}_{20}$  is found to be more sensitive to temperature below RT and inert to a temperature change above RT. The first-principles technique employed in this study offers a promising research approach in predicting mechanical and thermal properties of future novel RHEAs.

## Conflicts of interest

The authors declare no conflict of interests.

## Acknowledgement

This research is partially supported by NSF EPSCoR CIMM project under Award No. 1541079, CIMM LINK project, and DoD support under contract No. W911NF1910005. The computational simulations were supported by the Louisiana Optical Network Infrastructure (LONI) with the supercomputer allocation loni.mat.bio12.

## REFERENCES

- [1] Tong CJ, Chen YL, Yeh JW, Lin SJ, Chen SK, Shun TT, et al. Microstructure characterization of Al<sub>x</sub>CoCrCuFeNi high-entropy alloy system with multiprincipal elements. *Metall Mater Trans A* 2005;36:881–93, <http://dx.doi.org/10.1007/s11661-005-0218-9>.
- [2] Lee C, Song G, Gao MC, Feng R, Chen P, Brechtel J, et al. Lattice distortion in a strong and ductile refractory high-entropy alloy. *Acta Mater* 2018;160:158–72, <http://dx.doi.org/10.1016/j.actamat.2018.08.053>.
- [3] Senkov ON, Wilks GB, Miracle DB, Chuang CP, Liaw PK. Refractory high-entropy alloys. *Intermetallics* 2010;18:1758–65, <http://dx.doi.org/10.1016/j.intermet.2010.05.014>.
- [4] Wang W-R-R, Wang W-R-L, Yeh J-W-W. Phases, microstructure and mechanical properties of Al<sub>x</sub>CoCrFeNi high-entropy alloys at elevated temperatures. *J Alloys Compd* 2014;589:143–52, <http://dx.doi.org/10.1016/j.jallcom.2013.11.084>.
- [5] Chou YL, Yeh JW, Shih HC. Effect of inhibitors on the critical pitting temperature of the high-entropy alloy Co<sub>1</sub> 5CrFeNi<sub>1</sub> 5Ti<sub>0</sub> 5Mo<sub>0</sub>. 1. *J Electrochem Soc* 2011;158:C246–251, <http://dx.doi.org/10.1149/1.3600348>.
- [6] Kao YF, Lee TD, Chen SK, Chang YS. Electrochemical passive properties of Al<sub>x</sub>CoCrFe Ni (x = 0, 0.25, 0.50, 1.00) alloys in sulfuric acids. *Corros Sci* 2010;52:1026–34, <http://dx.doi.org/10.1016/j.corsci.2009.11.028>.
- [7] Shi Y, Yang B, Xie X, Brechtel J, Dahmen KA, Liaw PK. Corrosion of Al<sub>x</sub>CoCrFeNi high-entropy alloys: Al-content and potential scan-rate dependent pitting behavior. *Corros Sci* 2017;119:33–45, <http://dx.doi.org/10.1016/j.corsci.2017.02.019>.
- [8] Senkov ON, Wilks GB, Scott JM, Miracle DB. Mechanical properties of Nb<sub>25</sub>Mo<sub>25</sub>Ta<sub>25</sub>W<sub>25</sub> and V<sub>20</sub>Nb<sub>20</sub>Mo<sub>20</sub>Ta<sub>20</sub>W<sub>20</sub> refractory high entropy alloys. *Intermetallics* 2011;19:698–706, <http://dx.doi.org/10.1016/j.intermet.2011.01.004>.
- [9] Senkov ON, Scott JM, Senkova SV, Miracle DB, Woodward CF. Microstructure and room temperature properties of a high-entropy TaNbHfZrTi alloy. *J Alloys Compd* 2011;509:6043–8, <http://dx.doi.org/10.1016/j.jallcom.2011.02.171>.
- [10] Wang SP, Xu J. TiZrNbTaMo high-entropy alloy designed for orthopedic implants: As-cast microstructure and mechanical properties. *Mater Sci Eng C* 2017;73:80–9, <http://dx.doi.org/10.1016/j.msec.2016.12.057>.
- [11] Yurchenko NY, Stepanov ND, Zherebtsov SV, Tikhonovsky MA, Salishchev GA. Structure and mechanical properties of B2 ordered refractory AlNbTiVZrx (x = 0–1.5) high-entropy alloys. *Mater Sci Eng A* 2017;704:82–90, <http://dx.doi.org/10.1016/j.msea.2017.08.019>.
- [12] Han ZD, Chen N, Zhao SF, Fan LW, Yang GN, Shao Y, et al. Effect of Ti additions on mechanical properties of NbMoTaW and VNbMoTaW refractory high entropy alloys. *Intermetallics* 2017;84:153–7, <http://dx.doi.org/10.1016/j.intermet.2017.01.007>.
- [13] Senkov ON, Woodward CF. Microstructure and properties of a refractory NbCrMo<sub>0.5</sub>Ta<sub>0.5</sub>TiZr alloy. *Mater Sci Eng A* 2011;529:311–20, <http://dx.doi.org/10.1016/j.msea.2011.09.033>.
- [14] Senkov ON, Senkova SV, Woodward C, Miracle DB. Low-density, refractory multi-principal element alloys of the Cr-Nb-Ti-V-Zr system: microstructure and phase analysis. *Acta Mater* 2013;61:1545–57, <http://dx.doi.org/10.1016/j.actamat.2012.11.032>.
- [15] Senkov ON, Senkova SV, Miracle DB, Woodward C. Mechanical properties of low-density, refractory multi-principal element alloys of the Cr-Nb-Ti-V-Zr system. *Mater Sci Eng A* 2013;565:51–62, <http://dx.doi.org/10.1016/j.msea.2012.12.018>.
- [16] Long Y, Liang X, Su K, Peng H, Li X. A fine-grained NbMoTaWVCr refractory high-entropy alloy with ultra-high strength: microstructural evolution and mechanical properties. *J Alloys Compd* 2019;780:607–17, <http://dx.doi.org/10.1016/j.jallcom.2018.11.318>.
- [17] Bei H. Multi-component solid solution alloys having high mixing entropy; 2015.
- [18] Lederer Y, Toher C, Vecchio KS, Curtarolo S. The search for high entropy alloys: a high-throughput ab-initio approach. *Acta Mater* 2018;159:364–83, <http://dx.doi.org/10.1016/j.actamat.2018.07.042>.
- [19] Senkov ON, Miller JD, Miracle DB, Woodward C. Accelerated exploration of multi-principal element alloys for structural applications. *Calphad* 2015;50:32–48, <http://dx.doi.org/10.1016/j.calphad.2015.04.009>.
- [20] Li Z, Pradeep KG, Deng Y, Raabe D, Tasan CC. Metastable high-entropy dual-phase alloys overcome the strength-ductility trade-off. *Nature* 2016;534:227–30, <http://dx.doi.org/10.1038/nature17981>.
- [21] Zhang Z, Mao MM, Wang J, Gludovatz B, Zhang Z, Mao SX, et al. Nanoscale origins of the damage tolerance of the high-entropy alloy CrMnFeCoNi. *Nat Commun* 2015;6:1–6, <http://dx.doi.org/10.1038/ncomms10143>.
- [22] Jo YH, Jung S, Choi WM, Sohn SS, Kim HS, Lee BJ, et al. Cryogenic strength improvement by utilizing room-temperature deformation twinning in a partially recrystallized VCrMnFeCoNi high-entropy alloy. *Nat Commun* 2017;8:1–8, <http://dx.doi.org/10.1038/ncomms15719>.
- [23] Sathiaraj GD, Bhattacharjee PP. Analysis of microstructure and microtexture during grain growth in low stacking fault energy equiatomic CoCrFeMnNi high entropy and Ni-60 wt.% Co alloys. *J Alloys Compd* 2015;637:267–76, <http://dx.doi.org/10.1016/j.jallcom.2015.02.184>.
- [24] Smith HR Jr, Hum JYK, Donlevy A, Cd'A H. The mechanical properties of some ductile niobium and tantalum base alloys prepared by electron beam melting. *J Less Common Met* 1960;2:69–75, [http://dx.doi.org/10.1016/0022-5088\(60\)90001-1](http://dx.doi.org/10.1016/0022-5088(60)90001-1).
- [25] Zhang Y, Zhou YJ, Lin JP, Chen GL, Liaw PK. Solid-solution phase formation rules for multi-component alloys. *Adv Eng Mater* 2008;10:534–8, <http://dx.doi.org/10.1002/adem.200700240>.
- [26] Zhang Y, Zuo TT, Tang Z, Gao MC, Dahmen KA, Liaw PK, et al. Microstructures and properties of high-entropy alloys. *Prog Mater Sci* 2014;61:1–93, <http://dx.doi.org/10.1016/j.pmatsci.2013.10.001>.
- [27] Takeuchi A, Inoue A. Classification of bulk metallic glasses by atomic size difference, heat of mixing and period of



- constituent elements and its application to characterization of the main alloying element. *Mater Trans* 2005;46:2817–29, <http://dx.doi.org/10.2320/matertrans.46.2817>.
- [28] Guo S, Ng C, Lu J, Liu CT. Effect of valence electron concentration on stability of fcc or bcc phase in high entropy alloys. *J Appl Phys* 2011;109:103505, <http://dx.doi.org/10.1063/1.3587228>.
- [29] Tsai MH, Tsai KY, Tsai CW, Lee C, Juan CC, Yeh JW. Criterion for sigma phase formation in Cr-and V-containing high-entropy alloys. *Mater Res Lett* 2013;1:207–12, <http://dx.doi.org/10.1080/21663831.2013.831382>.
- [30] Hohenberg P, Kohn W. Inhomogeneous electron gas. *Phys Rev* 1964;136:B864–71, <http://dx.doi.org/10.1103/PhysRev.136.B864>.
- [31] Kohn W, Sham LJ. Self-consistent equations including exchange and correlation effects. *Phys Rev* 1965;140:A1133–8, <http://dx.doi.org/10.1103/PhysRev.140.A1133>.
- [32] Kresse G, Furthmüller J. Efficient iterative schemes for ab initio total-energy calculations using a plane-wave basis set. *Phys Rev B* 1996;54:11169–86, <http://dx.doi.org/10.1103/PhysRevB.54.11169>.
- [33] I. S. D. Medea Materials Exploration and Design Analysis, CA, USA, <https://www.materialsdesign.com/medea-software> [accessed on 12 April 2020].
- [34] Blöchl PE. Projector augmented-wave method. *Phys Rev B* 1994;50:17953, <http://dx.doi.org/10.1103/PhysRevB.50.17953>.
- [35] Perdew JP, Burke K, Ernzerhof M. Generalized gradient approximation made simple. *Phys Rev Lett* 1996;77:3865, <http://dx.doi.org/10.1103/PhysRevLett.77.3865>.
- [36] Monkhorst HJ, Pack JD. Special points for Brillouin-zone integrations. *Phys Rev B* 1976;13:5188, <http://dx.doi.org/10.1103/PhysRevB.13.5188>.
- [37] Knuth ED. *The art of computer programming*. 3rd ed New York: Addison–Wesley; 1965.
- [38] Bhandari U, Zhang C, Yang S. Mechanical and thermal properties of low-density  $\text{Al}_{20+x}\text{Cr}_{20-x}\text{Mo}_{20-y}\text{Ti}_{20}\text{V}_{20+y}$ . *Crystals* 2020;10:27, <http://dx.doi.org/10.3390/cryst10040278>.
- [39] Le Page Y, Saxe P. Symmetry-general least-squares extraction of elastic coefficients from ab initio total energy calculations. *Phys Rev B* 2001;63:174103, <http://dx.doi.org/10.1103/PhysRevB.63.174103>.
- [40] Le Page Y, Saxe P. Symmetry-general least-squares extraction of elastic data for strained materials from ab initio calculations of stress. *Phys Rev B* 2002;65:104104, <http://dx.doi.org/10.1103/PhysRevB.65.104104>.
- [41] Zuo LI, Humbert MI, Esling CL. Elastic properties of polycrystals in the Voigt-Reuss–Hill approximation. *J Appl Crystallogr* 1992;25:751–5, <http://dx.doi.org/10.1107/S0021889892004874>.
- [42] Anderson OL. A simplified method for calculating the debye temperature from elastic constants. *J Phys Chem Solids* 1963;24:909–17, [http://dx.doi.org/10.1016/0022-3697\(63\)90067-2](http://dx.doi.org/10.1016/0022-3697(63)90067-2).
- [43] Mayer B, Anton H, Bott E, Methfessel M, Sticht J, Harris J, et al. Ab-initio calculation of the elastic constants and thermal expansion coefficients of Laves phases. *Intermetallics* 2003;11:23–32, [http://dx.doi.org/10.1016/S0966-9795\(02\)00127-9](http://dx.doi.org/10.1016/S0966-9795(02)00127-9).
- [44] Guo S, Hu Q, Ng C, Liu CT. More than entropy in high-entropy alloys: forming solid solutions or amorphous phase. *Intermetallics* 2013;41:96–103, <http://dx.doi.org/10.1016/j.intermet.2013.05.002>.
- [45] Yang X, Zhang Y. Prediction of high-entropy stabilized solid-solution in multi- component alloys. *Mater Chem Phys* 2012;132:233–8, <http://dx.doi.org/10.1016/j.matchemphys.2011.11.021>.
- [46] Pugh SFXCII. Relations between the elastic moduli and the plastic properties of polycrystalline pure metals. London, Edinburgh, Dublin. *Philos Mag J Sci* 1954;45:823–43, <http://dx.doi.org/10.1080/14786440808520496>.
- [47] Pettifor DG. Theoretical predictions of structure and related properties of intermetallics. *Mater Sci Technol* 1992;8:345–9, <http://dx.doi.org/10.1179/mst.1992.8.4.345>.
- [48] Huang S, Li X, Huang H, Holmström E, Vitos L. Mechanical performance of FeCrCoMnAlx high-entropy alloys from first-principle. *Mater Chem Phys* 2018;210:37–42, <http://dx.doi.org/10.1016/j.matchemphys.2017.08.061>.
- [49] Chen X-Q-Q, Niu H, Li D, Li Y. Modeling hardness of polycrystalline materials and bulk metallic glasses. *Intermetallics* 2011;19:1275–81, <http://dx.doi.org/10.1016/j.intermet.2011.03.026>.
- [50] Sarker P, Harrington T, Toher C, Oses C, Samiee M, Maria J-P-P, et al. High-entropy high- hardness metal carbides discovered by entropy descriptors. *Nat Commun* 2018;9:4980, <http://dx.doi.org/10.1038/s41467-018-07160-7>.
- [51] Juan CC, Tsai MH, Tsai CW, Lin CM, Wang WR, Yang CC, et al. Enhanced mechanical properties of HfMoTaTiZr and HfMoNbTaTiZr refractory high-entropy alloys. *Intermetallics* 2015;62:76–83, <http://dx.doi.org/10.1016/j.intermet.2015.03.013>.
- [52] Dong Y, Zhou K, Lu Y, Gao X, Wang T, Li T. Effect of vanadium addition on the microstructure and properties of AlCoCrFeNi high entropy alloy. *Mater Des* 2014;57:67–72, <http://dx.doi.org/10.1016/j.matdes.2013.12.048>.